# Electrical detection of ambipolar acoustic carrier transport by surface acoustic waves

S. J. Jiao,[a] P. D. Batista, K. Biermann, R. Hey, and P. V. Santos[b]
*Paul-Drude-Institut für Festkörperelektronik, Hausvogteiplatz 5-7, 10117 Berlin, Germany*

(Received 4 June 2009; accepted 28 July 2009; published online 4 September 2009)

We have investigated the efficiency of the ambipolar transport of photogenerated electrons and holes in (Al,Ga)As structures by surface acoustic waves (SAWs). In the experiments, the photogenerated electrons and holes transported by the SAW are collected by a lateral *p-i-n* junction and detected by electrometers. Carrier recombination during transport was also studied by detecting the photoluminescence emitted along the SAW path by the transported carriers. We show that the acoustic transport efficiency improves by using biased metallic guides along the SAW beam to create independent transport channels for electrons and holes. By optimizing the photon absorption efficiency and the amplitude of the acoustic fields, we demonstrated overall transport efficiencies above 85% for transport lengths on the order of 300 $\mu$m. © *2009 American Institute of Physics*. [doi:10.1063/1.3211861]

## I. INTRODUCTION

The piezoelectric potential of a surface acoustic wave ($\Phi_{SAW}$) in a piezoelectric semiconductor creates a mobile type II modulation of the band edges, which strongly interacts with charge carriers. Electrons (holes) are captured at the position of minimum (maximum) potential and transported with the acoustic velocity ($v_{SAW}$). The acoustically induced carrier transport (ACT) is classified into two major categories according to the types of transported carriers. In unipolar ACT, where only one type of carrier (mostly electrons) is transported, the charge is normally injected from a doped region and electrically detected after transport using doped regions along the semiconductor surface.[1] In the ambipolar transport, in contrast, both electrons and holes are transported simultaneously trapped in the positive and negative potential wells created by $\Phi_{SAW}$. Most of the studies of the ambipolar ACT to date have been carried out by using light to generate electrons and holes and by collecting the photoluminescence (PL) emitted through recombination to map the carrier distribution along the semiconductor transport channel. Such studies have been performed in quantum wells[2] as well as quantum wires[3] and dots.[4] A few studies have also demonstrated electrical detection of the acoustically transported carriers using metal guides deposited on the sample surface.[5]

The ambipolar ACT has been proposed for a number of applications including photonic switches,[6] spin,[7] and exciton manipulation[8] as well as for the generation and detection of single photons.[9,10] Recently, we have proposed a new concept for a single-photon detector (SPD) based on the combination of ambipolar ACT with charge detection by radio-frequency single-electron transistors (rf-SETs).[11] The operation principle of this acoustoelectric SPD (ACDET) is illustrated in Fig. 1. The incoming photons are absorbed in a region (dashed circle) of the GaAs active layer subjected to a SAW field generated by an interdigital transducer (IDT). In order to increase the photon absorption efficiency, the active layer is sandwiched between two Bragg mirrors (BMs) to form an optical cavity. Electrons and holes generated by an incident light beam are spatially separated along the *x*- and *y*-directions by the type II SAW piezoelectric field and by the lateral electric field produced by metallic guides placed along the SAW channel, respectively. The moving SAW field then transports them underneath the guides toward narrow charge detection areas, where they can be collected in doped regions and detected by electrometers. Alternatively, rf-SETs can be used to detect the transported charge. The high charge sensitivity of the rf-SETs is expected to make photon-number resolving (PNR) possible, which is an important feature for quantum information processing applications including recent proposals for quantum computation with linear optical elements. Alternative approaches for the realization of PNR-SPD include avalanche photodiodes,[12–15] quantum dot transistors,[16,17] and superconducting bolometers.[18,19] A distinctive feature of the scheme in Fig. 1 relies on the spatial separation of the photon absorption and detection regions, which allows them for independent optimization to achieve

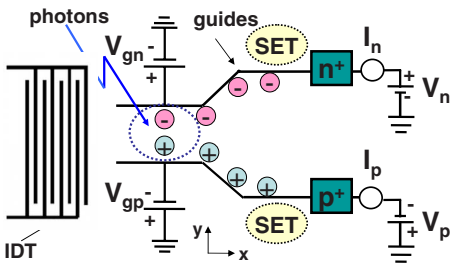


FIG. 1. (Color online) Schematic diagram of the single-photon detection process using acoustic transport (Ref. 11). The incoming photons are absorbed in the region indicated by the dashed circle, which lies within the path of a SAW generated by an IDT. Electrons and holes are attracted to polarized metal guides and transported underneath them toward narrow charge detection areas (*n*- and *p*-type contacts), where they are detected by electrometers. For single-photon sensitivity, rf-SETs are used to detect the transported charge.

[a]Electronic mail: shujiejiao@gmail.com.
[b]Electronic mail: santos@pdi-berlin.de.

 

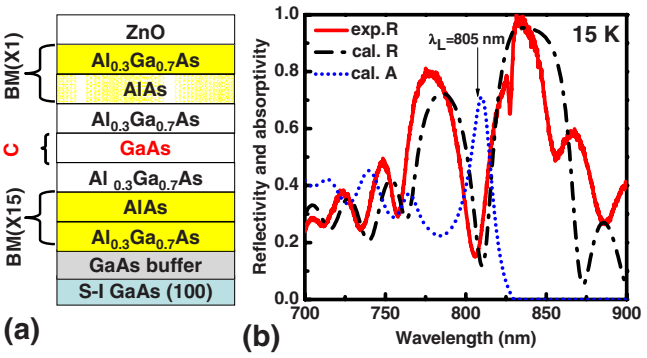


FIG. 2. (Color online) (a) Layer structure and (b) optical reflectivity measured at 15 K (solid line). The dashed-dotted and dotted lines show the calculated reflectivity and absorptivity spectra, respectively.

high quantum efficiencies. In this way, the photon absorption area can be made sufficiently large in order to provide high photon collection efficiencies. The detection region, in contrast, can be made very small to ensure high charge sensitivity by the rf-SETs.

The ACDET requires efficient photon absorption and acoustic carrier transport for its operation. In this work, we address these issues in devices where the charge transported in a GaAs channel is collected by a lateral *p-i-n* junction and subsequently detected by electrometers. We show that the photon-to-charge conversion increases drastically by embedding the GaAs transport channel in an asymmetric microcavity. The carrier transport and collection efficiencies are studied as a function of the acoustic power and of the voltages applied to the guides and contacts. In addition, spatially resolved PL is used to investigate the role of radiative recombination centers along the transport path. We show that the devices can achieve overall photon-to-collected-charge efficiencies exceeding 85% after ACT over 300 $\mu$m, thus demonstrating the feasibility of ACT for applications in devices for quantum information process.

The article is organized as follows. Section II describes the design of layer structures for high optical absorption as well as the steps for the photolithographic fabrication of the samples. The experimental results obtained using PL and the electrical measurements are summarized in Secs. III A and III B, respectively. The main conclusions are summarized in Sec. IV

## II. EXPERIMENTAL DETAILS

In this section, we describe the design considerations and the deposition of the layer structure of the detector by molecular beam epitaxy (MBE). We then discuss the photolithographic process for the fabrication of lateral *p-i-n* junction, metal guides, and acoustic transducers.

### A. Layer structure

A schematic diagram of the (Al,Ga)As detector layer structure grown by MBE is shown in Fig. 2(a). Here, the active 448-nm-thick GaAs transport layer is sandwiched between two BM stacks of AlAs and $Al_xGa_{1-x}$ As layers with $x=0.3$ to form an asymmetric optical microcavity. The latter concentrates incoming photons with the operation wavelength of $\lambda=805$ nm within the active GaAs layer, thus significantly increasing the photon absorption. The lower BM consists of 15 periods of AlAs and $Al_{0.3}Ga_{0.7}As$ $\lambda/4$ layers producing a reflection band centered on the operation wavelength. In order to improve the efficiency of the guiding electrodes, it is important to keep the transport layer close to the surface. Due to this constraint, the upper BM consists of only one pair of AlAs and $Al_{0.3}Ga_{0.7}As$ layers with thickness optimized to enhance the absorption in the $2\lambda$-thick GaAs active layer. As will be discussed in detail in the following section, we have deposited a $\lambda$-thick piezoelectric ZnO layer over the whole structure in order to increase the amplitude of the SAW piezoelectric potential. Figure 2(b) compares the reflectivity spectrum measured at 15 K with calculations for the reflectivity and absorptivity of the layers. The microcavity structure creates a region of minimum reflection centered around 805 nm, where a fraction of approximately 70% of the incoming photons is absorbed in the GaAs active layer. Since the microcavity resonance is blueshifted with respect to the GaAs bandgap, the optical microcavity is also expected to reduce the probability of electron-hole recombination during acoustic transport. This effect, however, only plays a minor role in the present structures due to the relatively low quality factor of the cavity.

The reduction in the Al content $x$ of the $Al_xGa_{1-x}As$ layers of the BMs can further increase the absorptivity at the operation wavelength (and therefore, the cavity quality factor). In fact, this approach was followed in the initial studies reported by us in Ref. 11, where we used $x=0.1$. We found, however, that $Al_xGa_{1-x}As$ layers with $x=0.1$ are photoconductive even for illumination with energies significantly below their bandgap (by as much as 80 meV at 15 K). This undesired photoconductivity makes the guides leaky, thereby hindering their guiding action.[11] Kim *et al.*[20] have attributed the subbandgap photoconductivity in $Al_xGa_{1-x}As$ alloys with low $x$ to percolation channels with low bandgap. We found that this unwanted photoconductivity (and guide leakage) can be avoided by increasing the alloy composition $x$ to 0.3.

### B. SAW generation

The SAWs have been generated by IDTs designed for an acoustic wavelength $\lambda_{SAW}=5.6$ $\mu$m. The split-finger IDTs consist of a finger grating with a periodicity of $\lambda_{SAW}/4$ leading to an acoustic resonance frequency of approximately 540 MHz. As illustrated in Fig. 2(a), the sample is coated with a piezoelectric ZnO film in order to improve the SAW generation efficiency. The expected enhancement in $\Phi_{SAW}$ induced by the ZnO coating is illustrated in the depth profiles of Fig. 3(a), which were calculated using an elastic continuum model for the layer structure. The calculations assume a linear acoustic power density $P_l=10$ W/m, where $P_l$ is the total acoustic power per unit length perpendicular to the SAW propagation direction. The origin $z=0$ of the depth scale corresponds to the position of the ZnO/(Al,Ga)As interface and the different layers can be identified by the mass density $\rho$ displayed in the right vertical scale. The amplitude of the piezoelectric field at the surface of the ZnO-coated structure exceeds the one in noncoated samples by a factor of

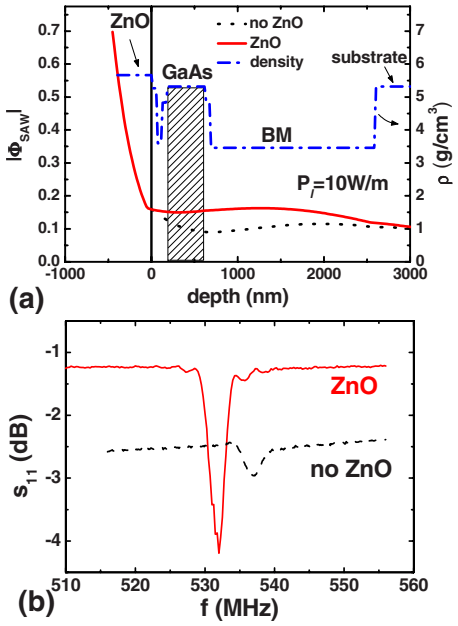


FIG. 3. (Color online) (a) Depth dependence of the amplitude of the piezoelectric field ($\Phi_{SAW}$) calculated for samples with and without a 400-nm-thick ZnO coating layer. The reference depth $z=0$ corresponds to the interface between the ZnO layer and the MBE-grown structure. The right scale displays the depth dependence of the mass density $\rho$. (b) Comparison of the rf-reflection coefficient $s_{11}$ for IDTs on samples with and without ZnO coating.

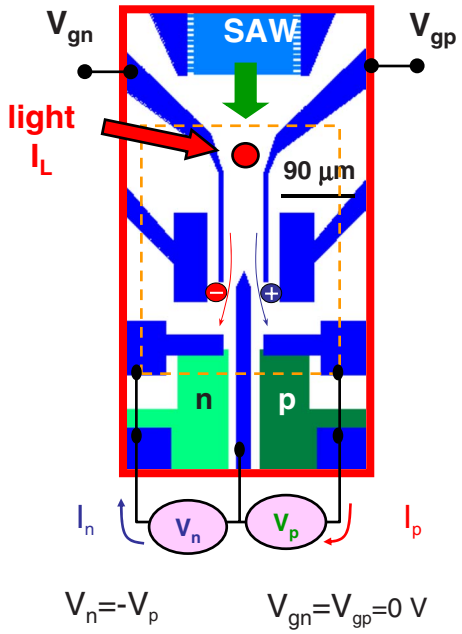


FIG. 4. (Color online) Top-view of the detector structure indicating the voltages applied to the different electrodes.

4.6, thus leading to a higher SAW generation efficiency. Also, for the same acoustic amplitude $P_l$, $\Phi_{SAW}$ is approximately 50% larger in the GaAs transport layer of the coated samples.

The enhancement in the SAW generation efficiency induced by ZnO coating is supported by measurements of the rf-power reflection coefficient ($s_{11}$) displayed in Fig. 3(b). The $s_{11}$-reflection dip associated with the electric-to-acoustic power conversion is much more accentuated in the ZnO-coated sample. The conversion efficiencies for the two samples were determined from the $s_{11}$ profiles to be 6.8% and 36%, respectively. We note that high conversion efficiency becomes particularly important to reduce the heating effects in devices with rf-SET detection, which operate at low temperatures.

### C. Photolithographic fabrication

The schematic diagram of Fig. 1 uses the electric field produced by the metallic guides to separate the photoexcited electrons and holes laterally, thereby avoiding their recombination during the transport to the *n*- and *p*-type contacts, respectively. We have experienced two main difficulties during the fabrication of these guides. First, the guides become electrically inactive when deposited directly on top of the ZnO film. This behavior is attributed to the pinning of the Fermi level by the high density of electronic states at the interface of ZnO and the MBE-grown layer structure. A similar effect has been reported for metal gates on $SiO_2$-coated GaAs samples.[21] As a result, the applied guide voltage drops across the ZnO layer rather than along the MBE-grown structure. To overcome this problem, the guides were evaporated directly on the (Al,Ga)As layers and prior to the ZnO deposition. They consist of a Ti (5 nm) and Au (50 nm) layer stack defined by a lift-off photolithographic process. The deposition of the guides as the first fabrication step after MBE growth also prevents the formation of processing-induced pinholes underneath the guides, which can induce leakage currents. Subsequently, *p*- and *n*-type contacts to the active channel were fabricated by wet chemical-etching the upper BM followed by the sputtering deposition of an Au–Be and of an Au–Ge alloy, respectively. The contacts were then alloyed at 450 °C for 10 min. In the third step, a 400-nm-thick piezoelectric ZnO layer was deposited by sputtering. The ZnO layer was then removed from the contact and guides areas by wet chemical-etching. In the last fabrication step, a lift-off metallization process defined the metal layers for the IDTs and electric contacts.

## III. RESULTS

All experiments were carried out in a microscope cryostat (temperatures between 5 and 20 K) with feed-throughs for electrical connections to the contacts, guides, and IDTs. The different voltages applied to the electrodes are indicated in Figs. 1 and 4, which display a top view of the photolithographic masks of the detector. The IDTs were excited by applying nominal rf-power levels ($P_{rf}$) ranging from −20 to 8 dBm. A laser beam focused onto an approximately 2-$\mu$m-wide laser spot (indicated by the circle) generates carriers within the path of the SAW beam. The photogenerated electrons and holes are attracted toward the *n*- and *p*-side guides subjected to voltages $V_{gn}$ and $V_{gp}$, respectively. The carriers are then transported underneath the guides toward the contacts subjected to voltages $V_n$ and $V_p$, respectively, where they are collected and detected by electrometers (leading to the currents $I_n$ and $I_p$, respectively).

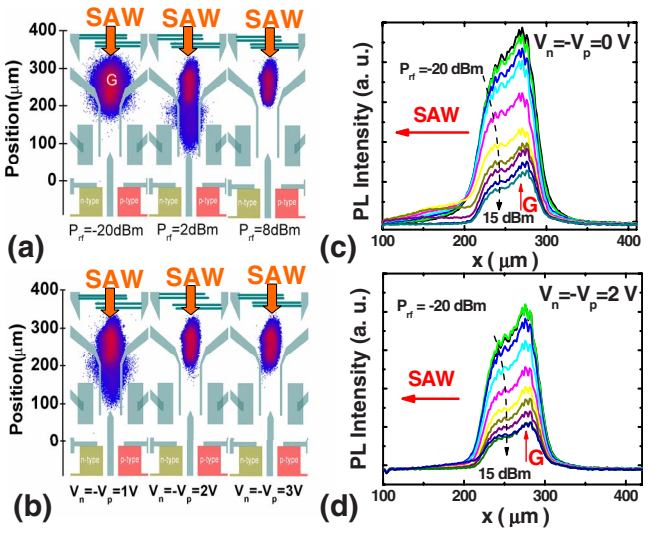


FIG. 5. (Color online) PL images recorded as a function of (a) the rf-power ($P_{rf}$) applied to the IDTs for fixed contact voltage $V_n=-V_p=1$ V and (b) the voltages $V_n=-V_p$ applied to the $n$- and $p$-type contacts for a fixed rf-power $P_{rf}=2$ dBm. The guides were kept at 0 V. The right panels display the PL intensity profiles along the transport path measured as a function of contact voltages (c) $V_n=-V_p=0$ V and (d) $V_n=-V_p=2$ V and rf power levels from −20 to 15 dBm. The arrows in (c) and (d) showing the PL intensity decrease with the increase of rf-power from −20 to 15 dBm.

### A. Optically detected carrier transport

Spatially resolved PL is a powerful tool to determine the efficiency of the electron-hole separation process as well as to map the spatial distribution of carriers during transport. In the PL experiments, a diode laser ($\lambda_L=765$ nm) was employed as excitation source and the PL emitted along the transport path detected with spatial resolution by a cooled charge coupled device camera.

The two-dimensional images of Fig. 5(a) display the PL emitted along the transport path as a function of the rf-power ($P_{rf}$) applied to the IDTs. The experiments were carried out by keeping the guides at zero potential and applying voltages of opposite polarities $V_n=-V_p=1$ V to the contacts. The SAW propagates from the top to the bottom of the diagrams, which were all drawn using the same color scale for the PL intensity. For low rf-power [$P_{rf}=-20$ dBm, leftmost image in Fig. 5(a)], the SAW field is not strong enough to separate the electron-hole pairs generated at point G and transport them away. The distribution of the PL is then determined by the diffusion of carriers away from G. With increasing $P_{rf}$, the PL spread along the transport path while the emission at G reduces, thus indicating carrier transport [center image for $P_{rf}=2$ dBm as well as Fig. 5(c)]. The transport is also confirmed by the increase in the current collected at the contacts. The substantial recombination along the path observed in Fig. 5(a) for $P_{rf}=2$ dBm is attributed to carrier trapping and subsequent recombination and indicates low transport efficiency. For higher acoustic powers ($P_{rf}=8$ dBm, rightmost plot), in contrast, the SAW becomes sufficiently strong to overcome trapping and prevent recombination during transport.

In addition to the SAW power, the contact voltages $V_n$ and $V_p$ applied to the contacts also play an important role in the transport efficiency. In order to illustrate this effect, Fig. 5(b) displays PL profiles recorded for $P_{rf}=2$ dBm and increasing contact voltages $V_n=-V_p$ (from the left to the right panel). The PL intensity along the transport path reduces significantly for large contact voltages. The reduction is assigned to the enhanced spatial separation and transport of carriers induced by carrier attraction to the $p$- and $n$-type contacts, which prevents recombination. The combined effects of the acoustic power $P_{rf}$ and contact voltages $V_n=-V_p$ on the transport efficiency are illustrated in Figs. 5(c) and 5(d). Here, the rf-power dependent PL integrated intensity across the SAW path is displayed as a function of the transport distance for $V_n=-V_p=0$ [Fig. 5(c)] and $V_n=-V_p=2$ V [Fig. 5(d)]. Under a SAW, the PL intensity reduces at the generation point and a tail develops along the SAW propagation direction. This tail, however, reduces as the transport becomes more efficient for high acoustic powers and/or contact voltages.

### B. Electrically detected carrier transport

The electrical characterization of the detector was carried out by generating carriers at the spot G in Fig. 6(a) using a pulsed laser beam with a wavelength of $\lambda_L=805$ nm, which is close to the minimum of the optical reflectivity in Fig. 2(b). The laser pulse width is 100 ps and the repetition rate can be set between 10 and 40 MHz. Voltages of opposite polarities were applied to the $n$- and $p$-type contacts (i.e., $V_n=-V_p$), as well as to the guides (i.e., $V_{gn}=-V_{gp}$). The current collected at the $n$-type ($I_n$) and $p$-type ($I_p$) contacts were measured using electrometers, as shown in Fig. 4. The guide currents have also been recorded ($I_{gn}$,$I_{gp}$). For an ideal device, one expects to have

$$I_{gn}=I_{gp}=0, \tag{1}$$

$$I_{Total}=I_n+I_p+I_{gn}+I_{gp}=0. \tag{2}$$

The last expression reflects the fact that an equal number of electrons and holes are generated by the incoming photons.

We define the photon collection efficiency (or detector quantum efficiency) $\eta$ as the ratio between the number (per unit time) of electrically detected electrons (or holes) ($N^c_{e,h}$) and the incident photons flux ($N_{ph}$) according to

$$\eta=\frac{N^c_{e,h}}{N_{ph}}=\frac{\hbar\omega_L}{e}\frac{I_{p(n)}}{I_L}, \tag{3}$$

where $I_L$ is the incident light intensity. Note that $\eta$ represents a lower limit for the internal quantum efficiency, since it does not take into account losses due to reflection or incomplete photon absorption in the active layer.

Figure 6(b) displays the evolution of the contact currents $I_n$ and $I_p$ as a function of acoustic power measured by illuminating the sample on the spot G indicated in Fig. 6(a). The right scale of the plots shows the transport efficiency obtained from Eq. (3). The guides were kept at 0 V during this measurement. Note that $I_n$ and $I_p$ have the same amplitude and different polarities, as expected from the collection of the same amount of photogenerated electrons and holes. In the absence of illumination, the reverse current remains very small (<10 pA) in the interval of reverse bias −4 V<($V_p$

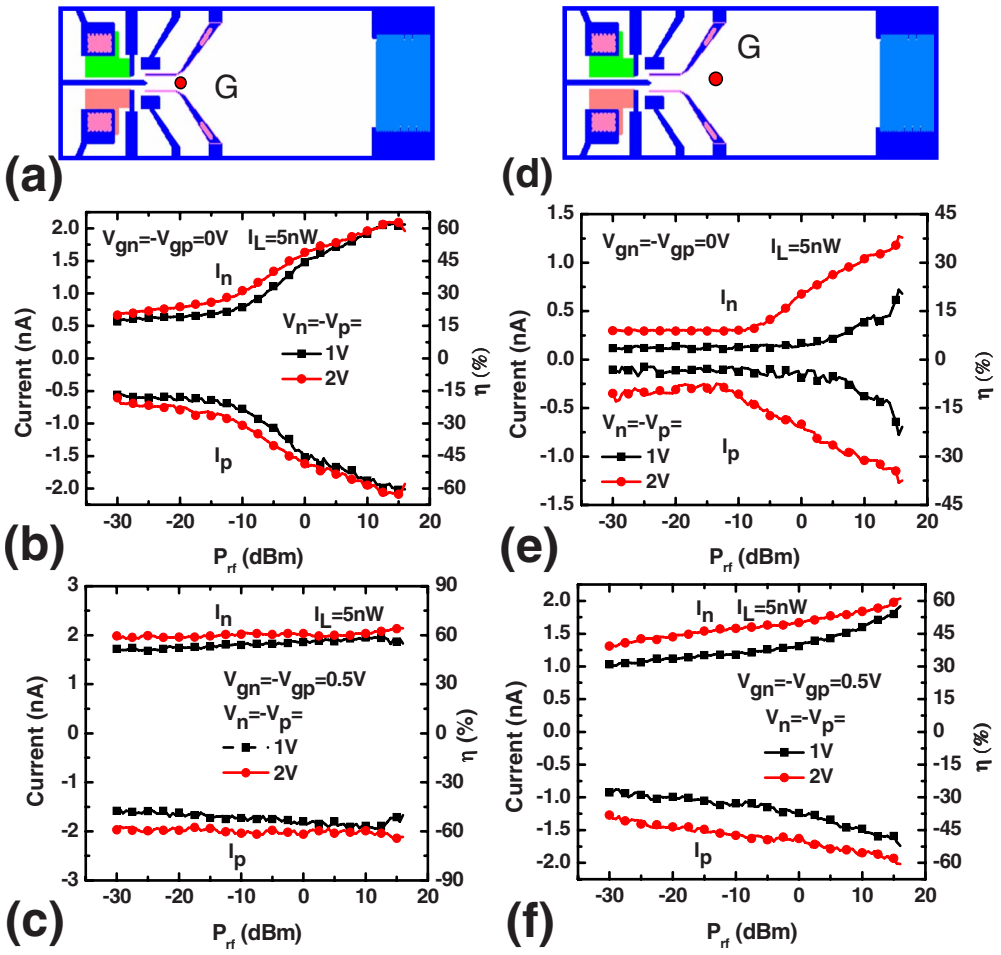


FIG. 6. (Color online) (a) Schematic diagram of the detector displaying the position of the light generation spot situated close to the guides. Dependence of the collected currents $I_n$ and $I_p$ on acoustic power $P_{rf}$ for illumination levels $I_L$=5 nW recorded with (b) $V_{gn}$=−$V_{gp}$=0 V and (c) $V_{gn}$=−$V_{gp}$=0.5 V. (e) and (f) show the corresponding dependence obtained when the illumination spot is placed away from the metal guides, as indicated in (d). The right vertical scales display the collection efficiency as defined by Eq. (3).

$-V_n)<0$ V. Under illumination, this current increases even in the absence of acoustic excitation due to the collection of photogenerated carriers that migrate to the contacts. For low rf powers ($P_{rf}<-15$ dBm), the acoustic field is too weak to transport the photogenerated electrons and holes, resulting in low collection efficiency. Acoustic transport takes place for $P_{rf}>-10$ dBm, leading to a maximum transport efficiency of approximately 60%.

The metallic guides have the important function of creating independent transport channels for electrons and holes parallel to the SAW and directing the carriers toward the detection regions. The guiding action has been investigated by recording the contact currents for different guiding voltages, as indicated by the results for $V_{gn}$=−$V_{gp}$=0.5 V in Fig. 6(c). Interestingly, when the guides are biased and the illumination spot placed close to them [in the position indicated in Fig. 6(a)], $I_n$=−$I_p$ reach values close to their maximum even in the absence of acoustic excitation. In this case, the acoustic wave only leads to a moderate further increase in current. The high collection efficiency observed under these conditions is attributed to the fact that the in-plane electric field generated by the guides efficiently attracts carriers toward them. The carriers then drift underneath the guides toward the collecting contacts, thereby preventing the build up of a space charge layer and ensuring high collection efficiency.

A high carrier collection in the absence of acoustic excitation only takes place when the generation spot is located close to the guides. When the carriers are created away from the guides [cf. Fig. 6(d)], the collection efficiency reduces significantly, as indicated by the curves recorded with $V_{gn}$=−$V_{gp}$=0 and 0.5 V in Figs. 6(e) and 6(f), respectively. The acoustic field is essential to improve carrier collection under these conditions. In the absence of guide voltages, the SAW increases the efficiency from 10% up to a maximum of approximately 40% [Fig. 6(e)]. Finally, the high efficiency values of Fig. 6(c) can be recovered under the simultaneous application of an acoustic wave and guide voltage, as illustrated in Fig. 6(f).

The dependence of the collection efficiency on the position of the illumination spots for different acoustic powers and guide voltages is summarized in Fig. 7. The results were obtained by recording the contact currents while scanning the laser spot along the line indicated in Fig. 7(a) using a fixed illumination intensity ($I_L$=5 nW) and contact voltages ($V_n$=−$V_p$=2 V). The dashed and solid lines show the mea-

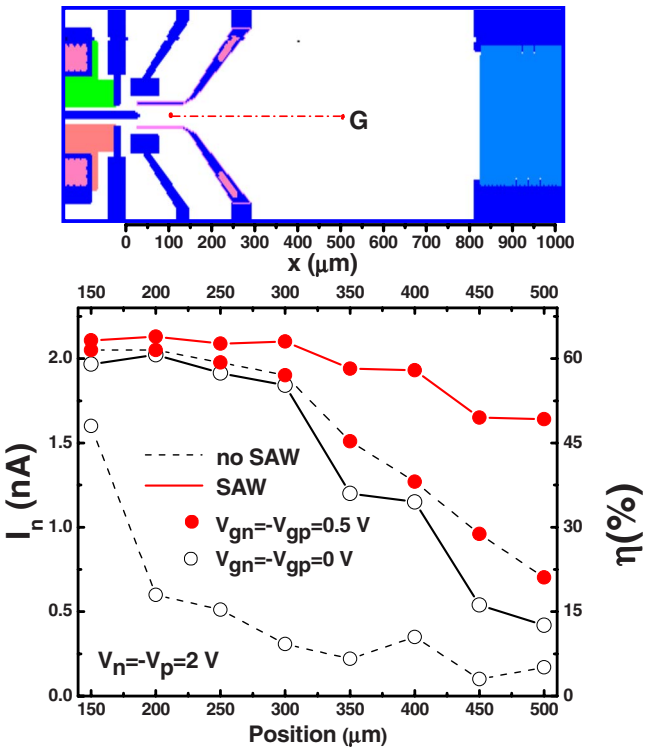


FIG. 7. (Color online) Dependence of contact current $I_n$ (=$-I_p$) on the position of the laser spot recorded for illumination intensity $I_L$=5 nW and contact voltages $V_n$=$-V_p$=2 V. The dashed and solid lines were measured without acoustic excitation and with $P_{rf}$=15 dBm, respectively. The open and solid symbols were recorded using $V_{gn}$=$-V_{gp}$=0 and 0.5 V, respectively.

sured $I_n$ without acoustic excitation and with $P_{rf}$=15 dBm, respectively. The open and solid symbols show the effects of guide voltages $V_{gn}$=$-V_{gp}$=0 and 0.5 V, respectively, on the collection efficiency (only $I_n$ is displayed since $I_p$=$-I_n$). As expected, the lowest collection efficiency is observed in the absence of acoustic excitation and guide bias $V_{gn}$=$-V_{gp}$=0 V. Here, a significant collection only occurs close to the contacts (corresponding to $x$=150 μm), where the carriers feel the field induced by the contact voltage. The application of either a SAW or of a guide voltage significantly improves the collection for illumination in-between the guides (150 $<x<$300 μm). The collection efficiency exceeds 60% for distances $x\leq$300 μm. By taking into account that only 70% of the photons are converted into electrons and holes [cf. Fig. 2(b)], these overall efficiencies lead to transport efficiencies above 85%. Finally, note that a high collection efficiency for illumination away from the guides ($x>$300 μm) can only be obtained under the simultaneous effects of a SAW and guide voltages.

We also investigated the effect of the illumination intensity on carrier collection. Figure 8 shows the dependence of the collected current $I_n$ on $P_{rf}$ measured for different laser illumination intensities $I_L$ (5, 15, and 50 nW) under guide voltages $V_{gn}$=$-V_{gp}$=0 (open symbols) and 0.5 V (solid symbols). The left vertical scale is normalized to the illumination intensity so as to become proportional to the efficiency $\eta$ indicated by the right vertical scale. For ratios $I_n/I_L$ $<$0.2 A/W, the efficiency $\eta$ does not depend on the illumination intensity. For higher ratios, however, a supralinear increase in $\eta$ with illumination intensity is observed, leading to values in excess of 100% for $I_L$=50 nW. We attributed this behavior to an avalanche multiplication process at the lateral *p-i-n* junction at large carrier densities. The avalanche process requires that the carriers gain enough energy from the lateral electric field of the *p-i-n* junction so as to excite new electron-hole pairs. In order to substantiate this assumption, we display in Fig. 9 the dependence of the detected current on the reverse bias applied to the contacts. These measurements were carried out without acoustic excitation by placing the light spot G as illustrated in Fig. 6(a) and keeping the guides at 0 V. In the absence of illumination, the reverse current remains very small ($<$10 pA) down to reverse voltages $V_{pn}$=$-$4 V. Under illumination, the photocurrent at low reverse biases (0 V$>V_{pn}>-$1.5 V) increases proportionally to the illumination intensity. For higher reverse voltages ($V_{pn}<-$1.5 V, which correspond to the bandgap of GaAs), in contrast, we observe a much stronger dependence on illumination intensity.[22] This behavior is consistent with the onset of avalanche multiplication, which can lead to collection efficiencies exceeding 100%.

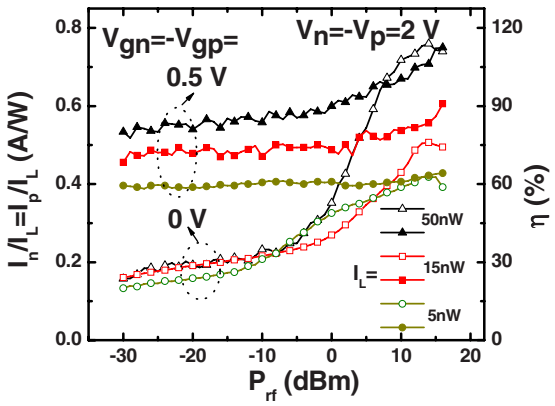


FIG. 8. (Color online) Contact current ($I_n$=$-I_p$, normalized to the light intensity $I_L$) as a function of acoustic power $P_{rf}$ recorded for $I_L$=5 nW, 15 and 50 nW using $V_n$=$-V_p$=2 V and $V_{gn}$=$-V_{gp}$=0 V (hollow symbols) 0.5 V (solid symbols).

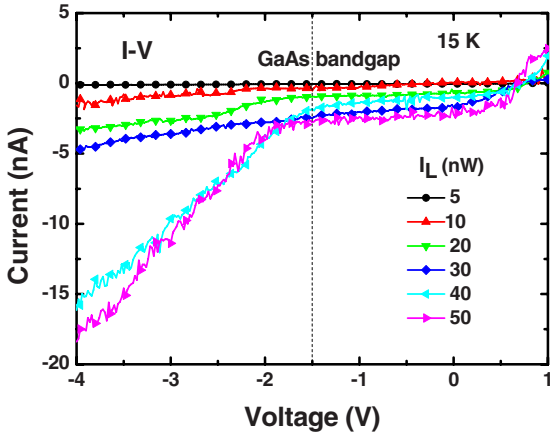


FIG. 9. (Color online) Current vs reverse voltage characteristics of the *p-i-n* junction recorded for laser spots in the absence of acoustic excitation of different intensities placed as in Fig. 6(a). The vertical dashed line indicate the voltage $V$ for which eV equals to GaAs bandgap.

## IV. CONCLUSION

We have investigated the electrical detection of the ambipolar transport of photogenerated electrons and holes by SAWs in (Al,Ga)As structures. The experiments were carried out in sample containing a GaAs channel inserted in an optical (Al,Ga)As microcavity to optimize light absorption. The samples were coated with a piezoelectric ZnO film to improve the electrical SAW generation using interdigital transducers as well as the piezoelectric SAW field. Acoustic carrier transport was directly observed by detecting the remote PL in spatially resolved PL images. The electrical detection employs a lateral *p-i-n* junction to collect simultaneously the transported electrons and holes. We show that the transport efficiency can be improved by using metallic guides to create separate transport channels for electrons and holes parallel to the SAW propagation direction. The overall quantum efficiency of the devices, defined by the ratio between collected carriers and incident photons, reaches 85%. We also show that detection sensitivities over 100% can be reached by taking advantage of avalanche multiplication at the collecting contacts. The high quantum efficiencies demonstrated here for acoustic transport over hundreds of micrometers open the way for the use of SAWs in high sensitivity photon detectors.

## ACKNOWLEDGMENTS

The European ACDET II program supports this work. We thank A. Tahraoui for discussion and W. Seidel and B. Drescher for assistance in the sample fabrication.

[1]V. I. Talyanskii, J. M. Shilton, M. Pepper, C. G. Smith, C. J. B. Ford, E. H. Linfield, D. A. Ritchie, and G. A. C. Jones, Phys. Rev. B **56**, 15180 (1997).
[2]C. Rocke, S. Zimmermann, A. Wixforth, J. P. Kotthaus, G. Böhm, and G. Weimann, Phys. Rev. Lett. **78**, 4099 (1997).
[3]F. Alsina, P. V. Santos, H.-P. Schönherr, W. Seidel, K. H. Ploog, and R. Nötzel, Phys. Rev. B **66**, 165330 (2002).
[4]C. Bödefeld, A. Wixforth, J. Toivonen, M. Sopanen, and H. Lipsanen, Phys. Status Solidi B **224**, 703 (2001).
[5]T. Palacios, F. Calle, and J. Grajal, Appl. Phys. Lett. **84**, 3166 (2004).
[6]V. I. Talyanskii, M. R. Graham, and H. E. Beere, Appl. Phys. Lett. **88**, 083501 (2006).
[7]O. D. D. Couto, F. Iikawa, J. A. H. Stotz, R. Hey, and P. V. Santos, Phys. Status Solidi C **3**, 4307 (2007).
[8]P. V. Santos, F. Alsina, J. A. H. Stotz, R. Hey, S. Eshlaghi, and A. D. Wieck, Phys. Rev. B **69**, 155318 (2004).
[9]C. Wiele, F. Haake, and Y. M. Golubev, Phys. Rev. A **60**, 4986 (1999).
[10]C. L. Foden, V. I. Talyanskii, G. J. Milburn, M. L. Leadbeater, and M. Pepper, Phys. Rev. A **62**, 011803 (2000).
[11]V. I. Talyanskii, J. A. H. Stotz, and P. V. Santos, Semicond. Sci. Technol. **22**, 209 (2007).
[12]J. Kim, S. Takeuchi, Y. Yamamoto, and H. Hogue, Appl. Phys. Lett. **74**, 902 (1999).
[13]M. D. Petroff, M. G. Stapelbroek, and W. A. Kleinhaus, Appl. Phys. Lett. **51**, 406 (1987).
[14]S. Takeuchi, J. Kim, Y. Yamamoto, and H. H. Hogue, Appl. Phys. Lett. **74**, 1063 (1999).
[15]B. E. Kardynał, Z. L. Yuan, and A. J. Shields, Nat. Photonics **2**, 425 (2008).
[16]E. J. Gansen, M. A. Rowe, M. B. Greene, D. Rosenberg, T. E. Harvey, M. Y. Su, R. H. Hadfield, S. W. Nam, and R. P. Mirin, Nat. Photonics **1**, 585 (2007).
[17]B. E. Kardynał, A. J. Shields, N. S. Beattie, I. Farrer, K. Cooper, and D. A. Ritchie, Appl. Phys. Lett. **84**, 419 (2004).
[18]A. Korneev, P. Kouminov, V. Matvienko, G. Chulkova, K. Smirnov, B. Voronov, G. N. Gol'tsman, M. Currie, W. Lo, and K. Wilsher, Appl. Phys. Lett. **84**, 5338 (2004).
[19]A. Divochiy, F. Marsili, D. Bitauld, A. Gaggero, R. Leoni, F. Mattioli, A. Korneev, V. Seleznev, N. Kaurova, O. Minaeva, G. Gol'tsman, K. G. Lagoudakis, M. Benkhaoul, F. Levy, and A. Fiore, Nat. Photonics **2**, 302 (2008).
[20]D. S. Kim, H. S. Ko, Y. M. Kim, S. J. Rhee, S. C. Hohng, Y. H. Yee, W. S. Kim, J. C. Woo, H. J. Choi, J. Ihm, D. H. Woo, and K. N. Kang, Phys. Rev. B **54**, 14580 (1996).
[21]J. Krauß, J. P. Kotthaus, A. Wixforth, M. Hanson, D. C. Driscoll, and A. C. Gossard, Appl. Phys. Lett. **85**, 5830 (2004).
[22]G. E. Bulman, D. R. Myers, T. E. Zipperian, L. R. Dawson, J. J. Wiczer, and R. M. Biefeld, Appl. Phys. Lett. **47**, 733 (1985).